IOP Publishing 2D Mater. 8 (2021) 025003 https://doi.org/10.1088/2053-1583/abce08

2D Materials

RECEIVED
5 September 2020

REVISED
22 November 2020

ACCEPTED FOR PUBLICATION
25 November 2020

PUBLISHED
17 December 2020

PAPER

Monolayer MoS_2 on sapphire: an azimuthal reflection high-energy electron diffraction perspective

Yu Xiang[1,2], Xin Sun[2], Lukas Valdman[3], Fu Zhang[4,5], Tanushree H Choudhury[4], Mikhail Chubarov[4], Joshua A Robinson[4,5], Joan M Redwing[4,5], Mauricio Terrones[4,5], Yuan Ma[6], Lei Gao[6], Morris A Washington[1,2], Toh-Ming Lu[1,2] and Gwo-Ching Wang[1,2]

[1] Physics, Applied Physics and Astronomy Department, Rensselaer Polytechnic Institute, Troy, NY 12180, United States of America
[2] The Center for Materials, Devices, and Integrated Systems, Rensselaer Polytechnic Institute, Troy, NY 12180, United States of America
[3] Material Science and Engineering Department, Rensselaer Polytechnic Institute, Troy, NY 12180, United States of America
[4] 2D Crystal Consortium, Materials Research Institute, The Pennsylvania State University, University Park, PA 16802, United States of America
[5] Department of Materials Science and Engineering, The Pennsylvania State University, University Park, PA 16802, United States of America
[6] Beijing Advanced Innovation Center for Materials Genome Engineering, Institute for Advanced Materials and Technology, University of Science and Technology Beijing, Beijing 100083, People's Republic of China

E-mail: yux1991@gmail.com **and** gaolei@ustb.edu.cn

Keywords: ARHEED, MoS_2, 2D materials, van der Waals epitaxy, 3D reciprocal space map, DFT

Supplementary material for this article is available online

Abstract

Molybdenum disulfide (MoS_2) on the *c*-plane sapphire has been a very popular system to study in the two-dimensional (2D) materials community. Bottom-up synthesis of monolayer (ML) MoS_2 with excellent electrical properties has been achieved on sapphire by various methods, making it a very promising candidate to be used in the next generation nano-electronic devices. However, large-area ML MoS_2 with comparable quality as the relatively small size exfoliated ML remains quite a challenge. To overcome this bottle neck, a comprehensive understanding of the structure of the as-grown ML material is an essential first step. Here, we report a detailed structural characterization of wafer-scale continuous epitaxial ML MoS_2 grown by metalorganic chemical vapor deposition on sapphire using an azimuthal reflection high-energy electron diffraction (ARHEED) technique. With ARHEED we can map not only 2D but also 3D reciprocal space structure of the ML statistically. From the oscillation in the ARHEED intensity profile along the vertical direction of the ML, we derived a real space distance of ~3 Å at the interface of ML and sapphire. Quantitative diffraction spot broadening analyses of the 3D reciprocal space map reveals low density defects and a small angular misalignment of orientation domains in ML MoS_2. Based on atomic force microscopy height distribution analysis, cross-section scanning transmission electron microscopy, and density functional theory calculations, we suggest that there exists a passivation layer between MoS_2 ML and sapphire substrate. This ARHEED methodology also has been applied to ML WS_2 and is expected to be applicable to other ML transition metal dichalcogenides on arbitrary crystalline or non-crystalline substrates.

1. Introduction

Transition metal dichalcogenides (TMDCs) have been intensively studied world-wide in recent years. Monolayer (ML) MoS_2 consisting of S–Mo–S trilayer is one of the pioneering and most studied semiconducting TMDCs [1–4]. A number of previous studies on bottom-up synthesized ML MoS_2 show similar morphologies: isolated triangular or hexagonal shape flakes with lateral size tens of microns scattered on a substrate [5–7]. The discontinuous flakes of ML MoS_2 discourage industrial applications. The top-down method using mechanical exfoliation of ML from bulk MoS_2 crystal [8, 9] can produce quality ML flake but they are still subject to limited size of ~100 microns. In contrast, wafer-scale continuous ML MoS_2 can now be grown by chemical vapor deposition (CVD) [10] or metalorganic CVD

© 2020 IOP Publishing Ltd

(MOCVD) [11]. The ML MoS_2 grown by MOCVD possesses several differences compared with that obtained by other methods. (a) Thickness: the MoS_2 samples grown by sulfurization of pre-deposited ultrathin Mo film or Mo foil [12–14] are ultrathin films (thickness > 5 nm) while our MOCVD grown MoS_2 on sapphire substrate is mostly ML. (b) Grain size: the ultrathin MoS_2 film grown by sulfurization have finite size (~tens of nm) grains aligned vertically with various tilt angles with respect to substrate normal. In contrast, our MoS_2 ML are all lying flat with hundreds of nm grain size. (c) Texture: the MoS_2 films are most likely textured polycrystalline when grown on amorphous SiO_2/Si substrate by sulfurization, while our MoS_2 ML is epitaxial. (d) Film continuity: before sulfurization, the Mo film and foil are continuous over a large area (wafer scale) but the sulfurized ultrathin MoS_2 films are neither continuous nor epitaxial over the large area size of starting Mo film or foil. Our ML MoS_2 and ML WS_2 grown by MOCVD is continuous over the wafer scale substrate. The good continuity and ultra-flatness of the MoS_2 ML grown by MOCVD facilitates the characterization by azimuthal reflection high-energy electron diffraction (ARHEED), and their large grain size and good crystallinity enable us to study the long-range order of these ML MoS_2 films. A continuous ML TMDC grown on a single crystal substrate is formed through the coalescence of individual domains with certain orientations. However, such CVD growth process may introduce a variety of defects in ML TMDCs [15–17] compared with the bulk TMDCs [18] partly due to lattice constant mismatch between TMDCs layer and the substrate as well as the imperfection of crystalline substrates. A good understanding of the structure of TMDCs and its interface with substrate is vital for improving the quality of CVD grown ML TMDCs. Therefore, quantitative characterization as well as synthesis of wafer-scale electronic grade ML TMDCs are essential for translating its electronic and optical properties into realistic applications [19].

In this work we report findings from the characterizations of MOCVD grown continuous epitaxial ML TMDCs, including MoS_2 and WS_2, on *c*-sapphire substrates. We used a technique, ARHEED [20–23], which is sensitive at detecting the long-range order in an ML. The ARHEED provides us an access to the 3D reciprocal space structure, which represents the macroscopic (~1 cm) statistical ensemble average of the structure and perfection of the MLs. We also used real-space imaging techniques scanning transmission electron microscopy (STEM) and atomic force microscopy (AFM) to help understanding the local structure.

Since ML MoS_2 and ML WS_2 have similar trilayer structures and their experimental results are qualitatively alike, we shall present findings from MoS_2 in the main text and WS_2 in the supplementary document. Our findings include: (a) the gap between the MoS_2 and the sapphire surface, which is defined as the distance from the bottom S atom in the ML MoS_2 to the top surface atomic layer of the sapphire surface, is measured to be ~3 Å by RHEED. Our cross-sectional STEM and AFM height scan measurements suggest the existence of a passivation layer at the MoS_2-sapphire interface. The formation of this passivation layer has been further understood through the density functional theory (DFT) calculations. We believe this maybe a general case for MOCVD grown TMDCs on sapphire substrates. (b) We constructed the 3D reciprocal space map of ML MoS_2/sapphire using ARHEED. Quantitative analysis of the 3D map data shows that the half-width-at-half-maxima (HWHMs) of the (00) diffraction and non-(00) diffraction spots are broader than the instrument response function width along the direction parallel to the surface. We have studied many factors that may broaden the diffraction peaks such as step atom density [24, 25], mosaic structure [26], and incommensurate domains, but altogether they could account for only a small part of the diffraction spot broadening. We attribute the rest of it to be the contribution from an angular dispersion of orientation domains that form the ML [16].

Similar results have been obtained from a second batch of ML MoS_2 and an ML WS_2 on sapphire substrates using the ARHEED method described above. We therefore believe this methodology is generic and can be applied to study other ML 2D materials on crystalline or non-crystalline substrates.

2. Results and discussion

2.1. Lattice constants measured from RHEED patterns of ML MoS_2 on sapphire

RHEED pattern is well known to reveal the symmetry of a surface structure. It can also reveal the lattice constants of ML. Figures 1(a) and (b) show RHEED patterns of ML MoS_2 on sapphire captured at two azimuthal angles 30° apart with the zone axis (ZA) along the $[2\bar{1}\bar{1}0]$ direction and the $[10\bar{1}0]$ direction, respectively. The straight through beam (S.T.) and shadowing edge (dashed line) are indicated on the RHEED patterns. The Miller indices (*hk*) of the diffraction streaks perpendicular to the shadowing edge are labeled. The scale bar has been calibrated previously by using a CdTe crystal with known lattice parameters [27]. The axes of the coordinate system in the reciprocal space are denoted by two perpendicular arrows on the bottom-right corner of each RHEED pattern, where $\mathbf{k}_{||}$ and $\mathbf{k}_{\perp}$ represent the momentum transfer parallel and perpendicular to the surface, respectively. The momentum transfer $\mathbf{k} = \mathbf{k}_{out} - \mathbf{k}_{in}$, where $\mathbf{k}_{out}$ and $\mathbf{k}_{in}$ are electron's outgoing and incoming wave vectors, respectively. Figures 1(c) and (d) are intensity profiles from RHEED patterns presented in figures 1(a) and (b) respectively. They are scanned along $\mathbf{k}_{||}$ at a fixed $\mathbf{k}_{\perp}$ of

5.1 Å^{-1}. A schematic is drawn on the top-right corner of each figure to illustrate the reciprocal lattice symmetry and the orientation of the line scan direction (the dashed line) relative to the reciprocal lattice (the red dots). The reciprocal space base vectors and ZA are also labeled as arrows in the insets. The nine peaks in figure 1(c) can be fitted by nine Gaussian functions after a smooth Gaussian background subtraction. From the fitted peak positions one can calculate the average peak-to-peak spacing $\Delta \mathbf{k}_{||} = 2.30 \pm 0.07$ Å^{-1}. This is related to the real space lattice constant a of MoS_2 through the reciprocal relationship $\Delta \mathbf{k}_{||} = \mathbf{G}(01) = 2\pi/d(01) = 2\pi/(\sqrt{3}a/2)$, where $\mathbf{G}(01)$ and $d(01)$ are reciprocal lattice vector and real space inter-atomic row spacing corresponding to the (01) diffraction spot, respectively. Therefore, the lattice constant can be determined to be $a = 4\pi/(\sqrt{3}\Delta \mathbf{k}_{||}) = 3.15 \pm 0.05$ Å, which is consistent with the bulk lattice constant of MoS_2 ($a = b = 3.1500$ Å, angle between unit vectors $\boldsymbol{a}$ and $\boldsymbol{b} = 60°$, ICDD reference code: 00-002-1133) within the experimental uncertainty. A similar analysis was performed for the intensity profile in figure 1(d) at a different azimuth angle 30° away from figure 1(c) and the lattice constant measured is $a = 3.14 \pm 0.09$ Å.

The upper curves of figures 1(e) and (f) show the intensity profiles scanned along $\mathbf{k}_{\perp}$ direction from the central (00) streak of the RHEED patterns shown in figures 1(a) and (b), respectively. In both cases, the intensities are not smoothly decaying as a function of $\mathbf{k}_{\perp}$. The intensity modulation is caused by the vertical structure of the MoS_2/sapphire system. Similar to the above procedures to determine in-plane lattice constants, one can estimate the interlayer spacing d in the out-of-plane direction. The mild intensity bumps in the upper curves in figures 1(e) and (f) became obvious peaks in the bottom curves after the subtraction of smooth backgrounds (the black dashed curves). This background is defined by connecting the diffraction intensity slightly to the outside of each 'bump' [28], with a smoothly decaying trend. The average reciprocal space spacing between two adjacent peaks is $\Delta \mathbf{k}_{\perp} = 2.08 \pm 0.04$ Å^{-1}. The intensity oscillation comes from the constructive and destructive interference of electron waves between atomic layers [29]. The period of oscillation $\Delta \mathbf{k}_{\perp}$ is inversely proportional to interlayer spacing d as $\Delta \mathbf{k}_{\perp} = 2\pi/d$. Therefore, the interlayer spacing between ML MoS_2 and sapphire surface $d = 2\pi/\Delta \mathbf{k}_{\perp} = 3.02 \pm 0.06$ Å. Similar results from another batch of ML MoS_2 on sapphire sample and an ML WS_2 on sapphire sample were presented in figures S1 (available online at stacks.iop.org/2DM/8/025003/mmedia) and S2, respectively, in the supplementary document. The origin of this d distance of ~3 Å will be discussed later.

2.2. AFM analysis of ML MoS_2 on sapphire

Next we examined the MoS_2–sapphire vertical separation distance through AFM height distribution measurements. Figure 2(a) shows an AFM image (5 μm × 5 μm) of MoS_2 that has a full ML coverage on the sapphire (0001) substrate with a low density of bilayer islands. A small area on the left side of this sample was scratched off by a stainless tweezer to expose the sapphire surface and create an irregular boundary between ML MoS_2 and sapphire surface. The scratched region shows terrace-step features similar to what was observed on a bare sapphire surface by others [30–33]. The terrace-step feature can also be seen in the ML region on the right side, which implies that the island grows conformally on the sapphire substrate [16, 34]. The density vs. height statistics [35] in figure 2(b) shows three peaks, which result from three height levels on the AFM image. The adjacent distance between two peaks indicates the continuous MoS_2 covered area to the scratched bare sapphire is 7.9 ± 0.1 Å, and the MoS_2 bilayer islands to the continuous MoS_2 ML covered area is 6.5 ± 0.1 Å. See an example of height line scan across the sample surface and a schematic ball model in figures 2(c) and (d), respectively. The 6.5 ± 0.1 Å is close to the expected distance from a MoS_2 bilayer to the MoS_2 ML (~6.1 Å). However, it is difficult to explain the 7.9 ± 0.1 Å without knowing the MoS_2–sapphire interface structure. Before looking into the interface, we compare our AFM results with the literature. The 'thicknesses' of CVD grown ML MoS_2 on *c*-sapphire substrate measured by AFM height scans have been reported many times in literature, ranging from 6 to 8.4 Å, as were summarized in table S1 in the supplementary document. But none of them has explained their measured value in detail. In fact, the interface structure of MoS_2 on sapphire is rather complicated due to the possible formation of a passivation layer [16] and the existence of sapphire terraces. We provide another more complicated AFM example in figure S3. Therefore, the definition of 'thickness' is open to interpretation. That is probably the reason why the literature reported values vary. For the time being, we assume there's a sulfur passivation layer, represented by orange balls, between sapphire and the ML MoS_2 in figure 2(d). It is this passivation layer that gives rise to the ~8 Å height measured by AFM. We will come back to this point in section 2.5, where more experimental evidence will be provided to support this hypothesis.

2.3. 3D reciprocal space map of ML MoS_2 on sapphire

Figure 3(a) shows a snapshot of the 3D reciprocal space map of the ML MoS_2/sapphire sample constructed from ARHEED patterns collected at 100 azimuthal angles. The axes of the coordinate system are momentum transfer in *x, y, z* directions, or namely, $\mathbf{k}_x$, $\mathbf{k}_y$, $\mathbf{k}_z$. Note that $\mathbf{k}_z$ is $\mathbf{k}_{\perp}$. The 3D map was constructed by stacking 2D reciprocal space maps [20] along the $\mathbf{k}_z$ direction. Figure 3(b) shows one such 2D reciprocal space map of ML MoS_2 at a fixed

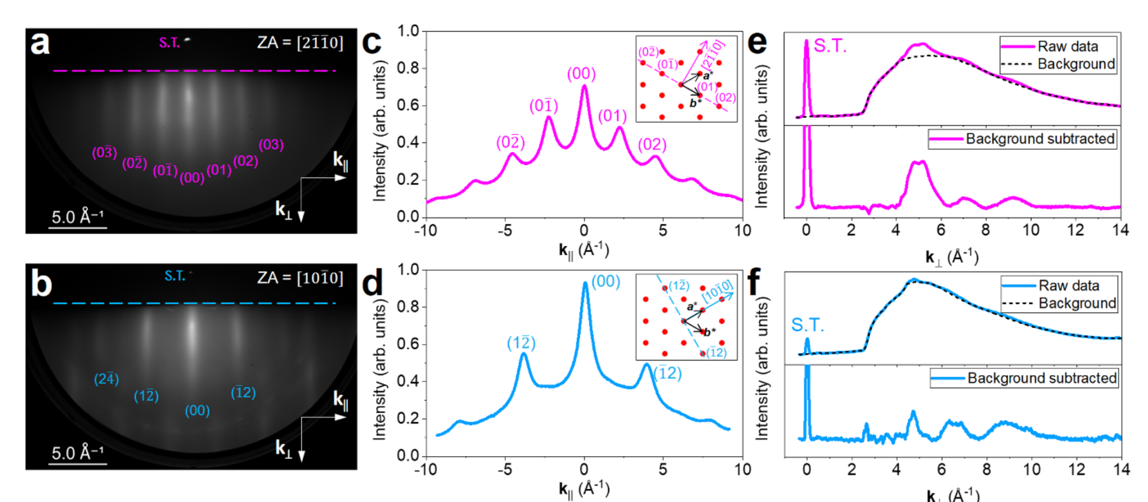

Figure 1. RHEED patterns along (a) ZA = $[2\bar{1}\bar{1}0]$ and (b) ZA = $[10\bar{1}0]$. The Miller index for each visible diffraction streak is labeled. The horizontal dashed line indicates the shadowing edge. The two arrows perpendicular to each other represents the $\mathbf{k}_{||}$ and $\mathbf{k}_{\perp}$ directions. (c) and (d) Line profiles scanned along $\mathbf{k}_{||}$ direction in the corresponding RHEED patterns shown in (a) and (b). The inset illustrates the scan direction (the dashed line) in the reciprocal lattice (the red dots) with base vectors $\boldsymbol{a}^*$ and $\boldsymbol{b}^*$. The ZA direction is indicated with a long arrow with Miller index labeled. (e) and (f) Line profiles of the (00) streak scanned along the $\mathbf{k}_{\perp}$ direction in the corresponding RHEED patterns shown in (a) and (b). The upper part of each figure shows the raw data (solid curve) and the smooth background (dashed curve) while the lower part shows the curve after the background subtraction.

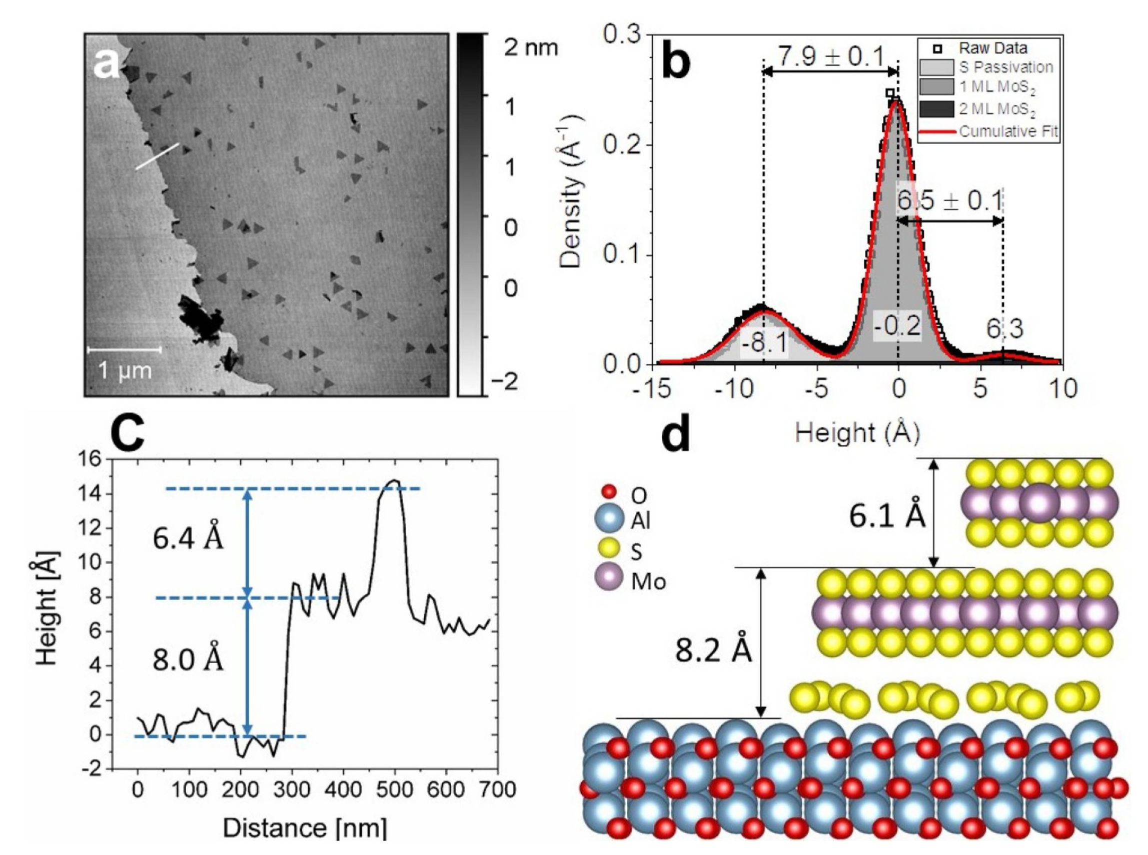

Figure 2. AFM characterization of MoS_2/sapphire (second batch). (a) The AFM image from the MoS_2/sapphire surface showing three distinct regions: a scratched region on the left, ML and bilayer regions on the right. (b) The height distribution of the AFM image shown in (a). The area under each peak equals to the coverage of each height level. (c) Height scan along the sample surface. (d) A schematic of ball model of (a).

value of $|\mathbf{k}_z| = 3.97$ Å^{-1} plotted as the intensity contour map in the polar coordinate system. The radial axis represents the momentum transfer parallel to the surface ($\mathbf{k}_{||}$) and the azimuthal angle φ ranges from 0° to 360°. Figure 3(c) is the simulated 2D reciprocal space map viewed along the [0001] direction of MoS_2. The symmetry and spots locations in the simulation are consistent with the

experimental 2D map shown in figure 3(b). Since the *c*-sapphire has the (0001) out-of-plane orientation, obviously, the out-of-plane epitaxial relationship is $[0001]_{MoS_2} \| [0001]_{sapphire}$. For the in-plane epitaxial relationship, azimuthal scans from $\{11\bar{2}0\}$ of MoS_2 and $\{11\bar{2}0\}$ of sapphire were measured by glancing incident x-ray diffraction (GIXRD) [36] as shown in figure 3(d). The three peaks from each material match each other. This suggests a parallel in-plane epitaxy: $[11\bar{2}0]_{MoS_2} \| [11\bar{2}0]_{sapphire}$, despite the ~34% in-plane lattice constant mismatch between MoS_2 (3.15 Å) and sapphire (4.78 Å).

2.4. Contributing factors to diffraction spot broadening

One noticeable feature from this 3D map is the in-plane broadening of the reciprocal rods. The HWHM of the (00) spot at a fixed value of $|\mathbf{k}_\perp|$ along a certain azimuthal direction is determined by first subtracting the linear background, then finding out the two positions ($\mathbf{k}_{\|}^{(1)}$, $\mathbf{k}_{\|}^{(2)}$) that correspond to half-maximum intensity of the remaining profile and finally obtaining HWHM = $|\mathbf{k}_{\|}^{(1)}-\mathbf{k}_{\|}^{(2)}|/2$. The process was repeated for all the $|\mathbf{k}_\perp|$ values and the azimuthal angles accessible in the 3D map. The red curve in figure 4(a) shows a slice of the measured HWHMs of the (00) spot vs. azimuthal angle at a fixed value of $|\mathbf{k}_\perp| = 3.97$ Å^{-1} from the ML MoS_2/sapphire sample. This $|\mathbf{k}_\perp|$ value is close to the in-phase condition between ML MoS_2 and sapphire. The in-plane directions of MoS_2 was indicated by the two arrows in figure 4(a), which was determined from the 2D map shown in figure 3(b). The HWHMs from 180° to 360° are replicas of that from 0° to 180° due to the fact that the (00) spot is symmetric about the center, and are therefore plotted as the dotted curve. The measured HWHMs range from ~0.4 Å^{-1} to ~0.6 Å^{-1}, which is much broader than the instrument response function width (h_{inst}) of ~0.1 Å^{-1} determined from the high-quality epitaxial graphene grown on copper substrate [21] (see figures S4(a) and (b)). Similar broadenings of the (00) spot and non-(00) spots are observed at other $|\mathbf{k}_\perp|$ values but are not presented here.

It is well known that various surface defects including point defects, step atoms and mosaic tilts could exist in any crystalline material. For TMDC MLs, the angular dispersion of domain orientations and its incommensurability with lattice-mismatched substrate need also to be considered. Each of them except point defects could contribute to the diffraction peak broadening [26]. They are elaborated separately in the following: random point defects itself will only increase the background intensity but not the broadening in the diffraction spots [26, 37]. For vacancy complex, the nearby atoms may relax locally and the distance between atoms could contract [17]. This produces microstrains which might account for part of the spot broadening. Our ML MoS_2 sample, however, has few defects as evidenced by the strong photoluminescence (PL) (figure S5(a)) [15] and the Raman spectra that is free of LA(M) peak at ~227 cm^{-1} (figure S5(b)) [38]. Therefore, the point defect induced broadening is ignored in this case.

2.4.1. Step atom density

The atomic scattering intensities from stepped surfaces have been studied by Spadacini *et al* [39]. According to the theory proposed there, the HWHM of the diffraction spot increases linearly as a function of the step atom density (figures S6(a1)–(a6) and (b)). In our case of MoS_2/sapphire, the step atom density (σ) can be estimated from the average terrace width of the sapphire surface to be $\sigma = 0.315$ nm/70 nm $\approx 0.5\%$. The average terrace width of the sapphire was calculated from the peak position in the fast Fourier transform (figure S7(a)) of the AFM image shown in figure S3(a) to be about 70 nm. The ~70 nm average terrace on sapphire is consistent with ~63 nm obtained from the sapphire annealed at 1000 °C in oxygen for 4 h by Yu *et al* [10]. Figure S7(b) shows a probability density distribution of the step inclination angle from the horizontal plane from the same AFM image. This indicates there exists a distribution of terrace width. According to HWHM (Å^{-1}) = 0.0073 × σ (%) in figure S6(b), those step atoms will result in ~0.004 Å^{-1} broadening in the diffraction spots, which is negligible. The experimentally observed MoS_2 domain sizes by high-resolution TEM are several hundred nanometers large [40].

2.4.2. Mosaic tilts

The statistical average of the mosaic tilt angle ($\theta/2$) across the surface can be found out by plotting the square of HWHM (h^2) as a function of the $\mathbf{k}_\perp^2$ using the data extracted from the 3D reciprocal space map, exactly the same way as how we determined the instrument response previously [28]. $h^2 = h_0^2 + h_{inst}^2 + \mathbf{k}_\perp^2 \tan^2(\theta/2)$. Therefore, both $\theta/2$ and the intrinsic broadening h_0 can be determined by doing a linear fit between h^2 and $\boldsymbol{k}_\perp{}^2$. Based on the analysis presented in figures S4(c) and (d) for the MoS_2/sapphire sample, $\theta/2$ is found to be about 2.4°. Since figure 4(a) was measured at $|\mathbf{k}_\perp| = 3.97$ Å^{-1}, therefore the contribution to the broadening from mosaic tilts is about $|\mathbf{k}_\perp| \tan(\theta/2) = 0.17$ Å^{-1}. This still cannot account for the ~0.4 A^{-1} broadening observed. A different experimental approach was carried out by Meyer *et al* to examine the surface corrugation of suspended graphene. They used the tilt function of TEM sample holder so that the Ewald sphere can reach diffraction spots at momentum transfer $\mathbf{k}_\perp > 0$ along the out-of-plane direction and measured the full-width-at-half-maximum of diffraction spots from the suspended graphene on a TEM grid. From the measured spot broadening as a function of tilt angle (effectively proportional to $\mathbf{k}_\perp$) from

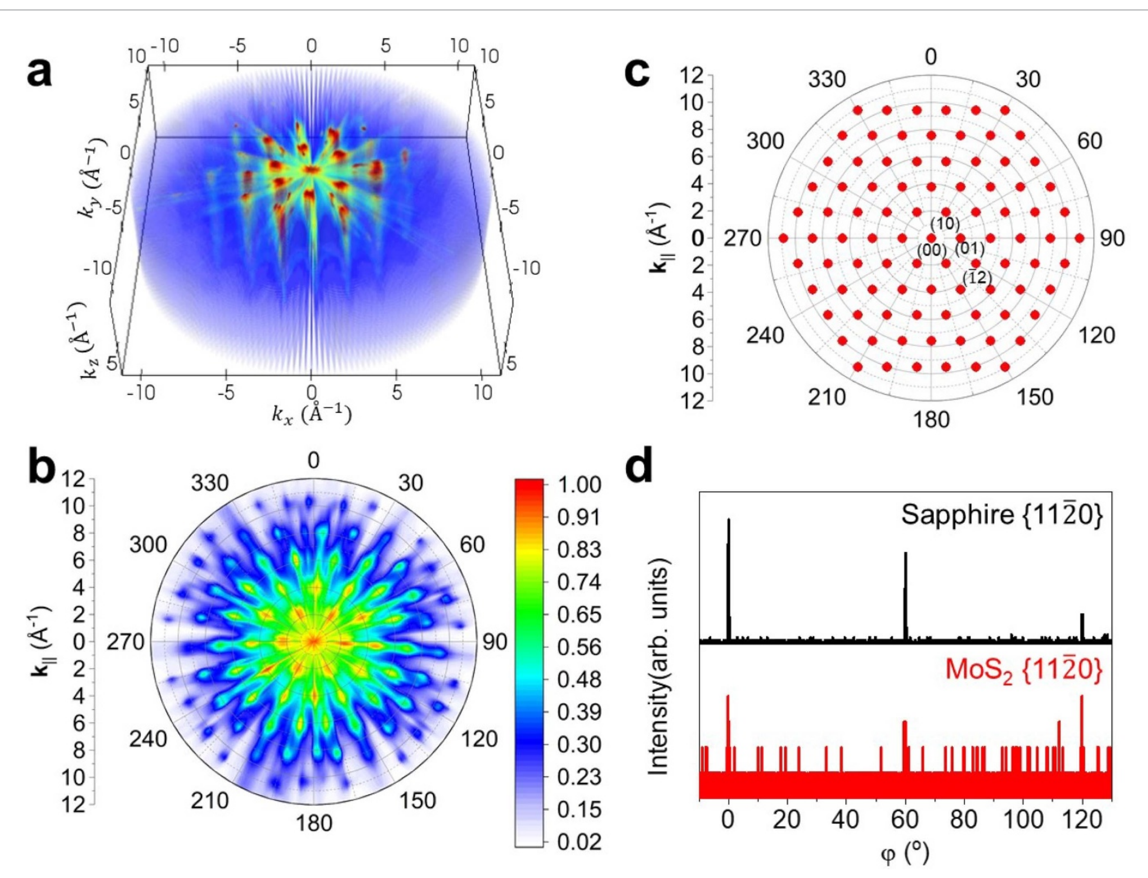

Figure 3. (a) A snapshot of the 3D reciprocal space map measured by ARHEED from MoS_2/sapphire. (b) Experimentally constructed ARHEED 2D reciprocal space map sliced from (a) at $|\mathbf{k}_z| = 3.97$ Å^{-1} and (c) the corresponding theoretical simulation. The radial axis represents the momentum transfer parallel to the surface ($\mathbf{k}_{||}$) and the azimuthal angle ranges from 0° to 360°. Some low order Miller indices are labeled on (c). (d) GIXRD azimuthal scans from sapphire [10] (upper) and MoS_2 sapphire 11$\bar{2}$0 (lower). Their peaks line up, which implies a parallel epitaxial relationship: $[11\bar{2}0]_{MoS_2} || [11\bar{2}0]_{sapphire}$.

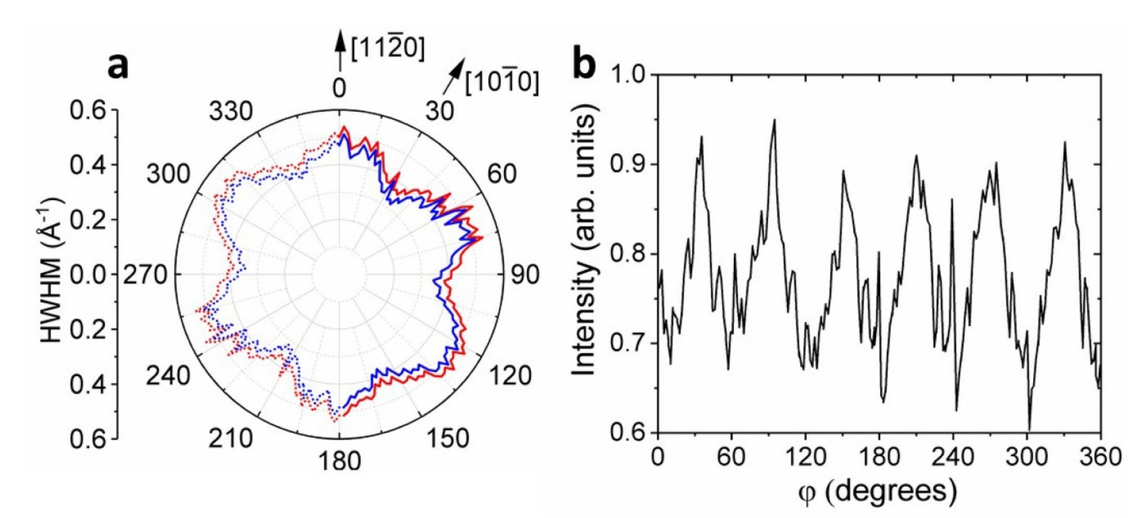

Figure 4. (a) A slice of the measured HWHMs of the (00) spot vs. azimuthal angle at a fixed $|\mathbf{k}_\perp| = 3.97$ Å^{-1} from the ML MoS_2/sapphire. The red and blue curves are before and after deconvolution with instrument response width and the mosaic tilt induced broadening, respectively. The in-plane directions of MoS_2 were indicated by the two arrows in (a). The average HWHM before and after deconvolution are 0.46 ± 0.05 Å^{-1} and 0.43 ± 0.05 Å^{-1}, respectively. (b) The azimuthal scan of the first order diffraction spots from MoS_2 ML on sapphire.

the graphene, they also found spot broadening from graphene and concluded that graphene is corrugated [41]. Our measured half-width-at-half maximum (h^2) vs. $\mathbf{k}_\perp^2$ of diffraction spot by RHEED are related to mosaic tilts from the ML MoS_2 and the broadening indicates that there is an out-of-plane corrugation. Note that the ML MoS_2 is grown by the conformal MOCVD technique on the substrate and

the perfection of the substrate may affect the mosaic tilt of the ML MoS_2.

2.4.3. Incommensurate domain boundaries

There is another potential contribution to the spot broadening in lattice mismatched systems, namely, the incommensurate domain boundaries. During the nucleation of the MoS_2 domains, they grow in size and meet to form domain boundaries [16, 22]. This is because the lattice constants between the MoS_2 (3.15 Å) and sapphire (4.76 Å) differ from each other. This type of domain boundaries can be described using a translational incommensurate domain model (or commonly referred to as the translational anti-phase domain model when the lattice constant of the overlayer is twice that of the substrate) [42]. A schematic showing the formation of various translational incommensurate domain boundaries in one dimension (1D) for MoS_2 on sapphire is presented in figures S6(c1)–(c4). The experimentally observed domain sizes can be as large as several hundred nanometers based on the high-resolution TEM image of ML MoS_2 [40] or as small as only a few nanometers according to the STEM images from ML WSe_2 on sapphire reported in the literature [16]. We calculated diffraction spot from several hundred nanometers large MoS_2 domain size on sapphire using either analytical 1D or numerical 2D translational incommensurate domain models. The spot broadening is extremely small. Only when the domain size decreases to a few nanometers (high boundary density) the spot broadening can reach the order of ~0.1 $Å^{-1}$. Therefore, for MoS_2 ML on sapphire the incommensurate domain boundaries have negligible contribution to the spot broadening.

2.4.4. Angular dispersion of orientation domains

The blue curve in figure 4(a) shows the HWHMs of the (00) spot vs. azimuthal angle after deconvoluting all the contributing factors mentioned above. The remaining spot broadening is at least ~ 0.3 $Å^{-1}$. From the in-plane 360° azimuthal scan of six first order diffraction spots in figure 4(b) we can see that the non-(00) spots also has a similar degree of broadening as seen in the 2D map in figure 3(b). Note that the instrument response width in the azimuthal direction is ~0.1 $Å^{-1}$, which is much narrower than that of the radial direction [43]. The average HWHMs of the six peaks is determined to be ~11.4 ± 1.2° by fitting each peak with a Gaussian function. This angular spread converts to a broadening of ~0.46 $Å^{-1}$. Through a similar method, the first order spots from a second batch MoS_2 ML sample showed an average HWHM of ~8.0° (shown in figure S1(f)). This converts to ~0.32 $Å^{-1}$, which means the second batch of MoS_2 has a smaller angular dispersion and thus better quality. This demonstrates a convenient way to characterize the angular dispersion in a material that could be useful for quality control purpose. A closer look at the first order peaks led us to observe a clear peak splitting of a few degrees (larger than the azimuthal step size of 1.8°) in figure 4(b) and more obvious in figure S1(f). This splitting indicates the existence of discrete orientational domains. A similar broadening of azimuthal scan of six first order spots 60° apart were also observed by Mo *et al* from their RHEED pattern in MOVPE grown MoS_2 on sapphire at 1000 °C. However, they observed broadened spots with no spot splitting in their six first order spots but observed additional spots appearing in the middle between 60° apart spots indicating a non-ideal parallel epitaxy [44].

We believe these broadening of the (00) and broadening/splitting of {10} peaks originate from the angular dispersions of the domain orientations. This dispersions are likely caused by the step edges and step edge meanderings of sapphire surface, which only occurs at high temperatures [30–32]. For the CVD grown ML WSe_2 on sapphire, it is shown that a step-edge-guided nucleation align the growth of 2D WSe_2 [34]. Therefore, if step edges of sapphire surface meander, which is true under the high growth temperature, the nucleated domains will not be perfectly aligned. A few degrees up to 15° of angular dispersion from MoS_2 ML flakes [7, 10, 45] and WSe_2 ML flakes [34] on sapphire were typical, measured from a small area (200 μm × 200 μm and 50 μm × 50 μm, respectively) using optical microscope. Our measured angular dispersion in domain orientations was detected by RHEED azimuthal scan from the wafer-scale area and is smaller than reported dispersions in literature. This indicates that our ML MoS_2 has better quality.

2.5. STEM images of ML MoS_2 on sapphire

The interpretation of the *d* value of ~3 Å from RHEED and ~8 Å from AFM height profile scan requires the knowledge about the details of the ML MoS_2–sapphire interface structure. For this purpose, an aberration-corrected STEM has been utilized to image the cross section, which was created by focused ion beam (FIB) cut, of this MoS_2–sapphire sample. Both high-angle annular dark field (HAADF) images with Z-contrast and conventional high-resolution transmission electron microscopy (HRTEM) bright field images with phase contrast were collected from this sample. Figures 5(a) and (b) show the cross-section view of HAADF-STEM and HRTEM images, respectively, without any image processing, along the $[1\bar{1}00]$ ZA of sapphire from the MoS_2/sapphire interface. From figure 5(a) we found that there exists a buffer layer (indicated by the yellow arrow in figure 5(a)) between the top bright layer (indicated by the blue arrow in figure 5(a)) and the substrate at the bottom. Figures 5(c) and (d) show the zoomed-in images from the region indicated by the yellow squares in figures 5(a) and (b), respectively, after applying a band-pass filter. They both show the existence of a buffer layer. From figures 5(c) and (d) we measured the gap

between the bottom of MoS_2 and this buffer layer to be about 3 Å.

Before we discuss the relation between this measured gap and the measured $d \sim 3$ Å from RHEED intensity profile vs. $\mathbf{k}_{\perp,}$ an immediate question one might ask is, what is the chemical composition and structure of this buffer layer? To address this question, we have measured energy-dispersive x-ray (EDX) mapping at the MoS_2–sapphire interface, as shown in figures S8(a)–(f). The EDX mapping is qualitatively consistent with our expectation: a MoS_2 layer on the top and the sapphire (Al_2O_3) substrate at the bottom. Due to the limited resolution, however, it is hard to make a clear conclusion about the chemical composition of this buffer layer. In the literature, a similar interface structure for epitaxial WSe_2 grown on sapphire has been reported by Lin *et al* [16]. They claimed that a Se passivation layer was formed at the interface to achieve van der Waals epitaxy of WSe_2 on sapphire. Since WSe_2 and MoS_2 have similar properties and they are both grown on sapphire substrates using the MOCVD method, we hypothesize that the buffer layer we observed in figure 5 is formed in a similar way as in their WSe_2/sapphire system, consisting of the chalcogen atoms, or S atoms, in our case.

2.6. First-principles density function theory calculations

We have also performed first-principles DFT calculations for an ML MoS_2 on Al-terminated sapphire with and without a S passivated layer to understand the RHEED, TEM and AFM measurements. See methods section for more details of DFT calculations. In brief, the calculated S atom adsorption energy E_{ad} is quite negative (−0.51 eV). This indicates that the S passivation layer formed at the sapphire termination is energetically feasible. The strong adsorption of S passivation layer could also be confirmed by the intensive charge transfer between the S passivation layer and sapphire as shown in positive value of bright red and orange cloud in figure 6(a). This indicates the S atoms form strong bonds with Al atoms when the S atoms are adsorbed on the sapphire. The interfacial interaction energy E_{int} between the MoS_2 and S passivated sapphire was also calculated. The MoS_2 layer was allowed to relax until the forces on all the relaxed atoms were less than 0.02 eV Å^{-1}. The calculated E_{int} is a negative small value (−13.3 meV Å^{-2}). This indicates that the MoS_2 layer could be adsorbed on the S passivated sapphire with a weak interaction. This interaction could be considered as van der Waals interaction. In contrast to figure 6(a), one can hardly see in figure 6(b) any color contrast related to charge transfer between MoS_2 and S atom implying weak bonds.

The Al-terminated sapphire is supported by low-energy electron diffraction [46] and glazing incident x-ray scattering [47] experiments. The DFT calculation results show that the formation of a S passivation layer of Al-terminated sapphire surface is more energetically feasible than just Al termination alone. Figure 5(e) displays the stabilized atomic structure for MoS_2 on S passivated sapphire surface viewed along the $[1\bar{1}00]$ ZA of sapphire. According to this stabilized structure from the DFT calculations, the average distance from the bottom of the MoS_2 ML to this S passivation layer is 3.06 Å and the S passivation layer to sapphire surface is 2.21 Å, which strike a close match with the value measured from the TEM images shown in figures 5(c) and (d). X-ray photoelectron spectroscopy (XPS) spectra of Mo, S, Al and O for chemical composition analysis are shown in figure S9. A comparison between the simulated HAADF-STEM image, the experimental HAADF-STEM image in figure 5(c) and the HRTEM image in figure 5(d) was shown in figures S10(a) and (c), respectively. By superposing the atomic ball model calculated from DFT shown in figure 5(e) on each of figures S10(d) and (f), we can clearly see that the DFT model agrees well with the TEM images. In addition, the DFT calculated ~2 Å from passivation layer to sapphire surface is consistent with the ~8 Å AFM height difference from the top of MoS_2 to sapphire. That comes from ~(3 + 3 + 2) Å from MoS_2, bottom of MoS_2 to passivation layer, and passivation layer to sapphire.

2.7. Kinematic RHEED intensity calculation

Next, we show the DFT calculated interface structure is consistent with the ~3 Å obtained from RHEED results. We have used the single scattering model to simulate the RHEED intensity profiles along the vertical momentum transfer $\mathbf{k}_{\perp}$ direction using the DFT calculated atomic structure shown in figure 5(e). Figure S11(a) shows a series of simulated RHEED intensity along $\mathbf{k}_{\perp}$ direction with various electron penetration depths. For grazing incident electron beam the penetration depth is shadow. The corresponding Fourier transform of the profiles in figure S11(a) are shown in figure S11(b). Note that the horizontal axis of those Fourier spectrum is $\mathrm{r}_{\perp}$, which is translated as the real-space periodicity that exists in the vertical direction of the DFT calculated structure shown in figure S11(c). The profiles in figures S11(a) and (b) are color coded with dark red being the shallowest penetration and purple being the deepest one. Their penetration positions are indicated by the dashed arrows connecting figures S11(b) and (c). From figure S11(b) we see that the peak around $\mathrm{r}_{\perp} = 3$ Å starts to show up when the electrons reach the bottom S atoms of the ML MoS_2. The peak intensity gets enhanced further when electrons reach the S passivation layer at the MoS_2–S–sapphire interface and then gradually becomes washed out when the electrons penetrate deeper into the sapphire substrate. This result suggests that indeed the DFT calculated structure shown in figure 5(e) can cause a periodicity of ~3 Å to be picked up by the RHEED intensity oscillation measurement.

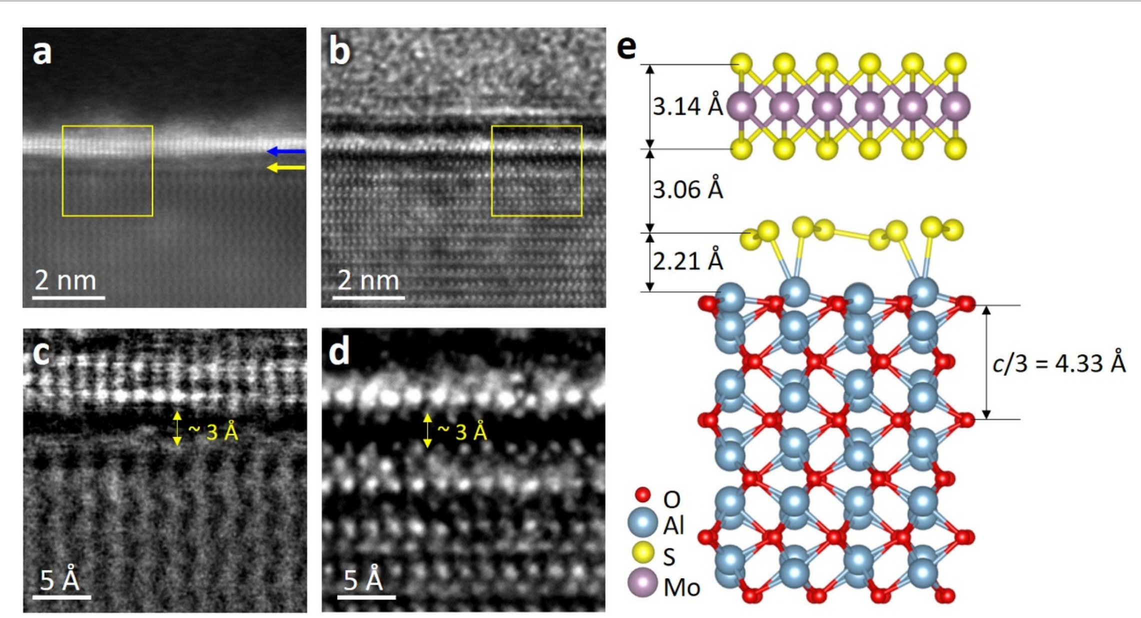

Figure 5. The cross-section views of (a) HAADF-STEM and (b) HRTEM images along the [1$\bar{1}$00] ZA of sapphire from the MoS_2/sapphire interface without any image processing. The blue and yellow arrows in (a) indicate the interface of MoS_2 and sapphire. The zoomed-in view of (c) HAADF-STEM and (d) HRTEM images from the yellow square denoted in (a) and (b), respectively. The distance measured from the bottom of the MoS_2 to the buffer layer is ~3 Å, as are denoted on the figures. (e) The DFT calculated stabilized atomic structure of an ML MoS_2 on a S passivated sapphire. The critical distances and sapphire interplanar distance (c/3) are labeled in this schematic.

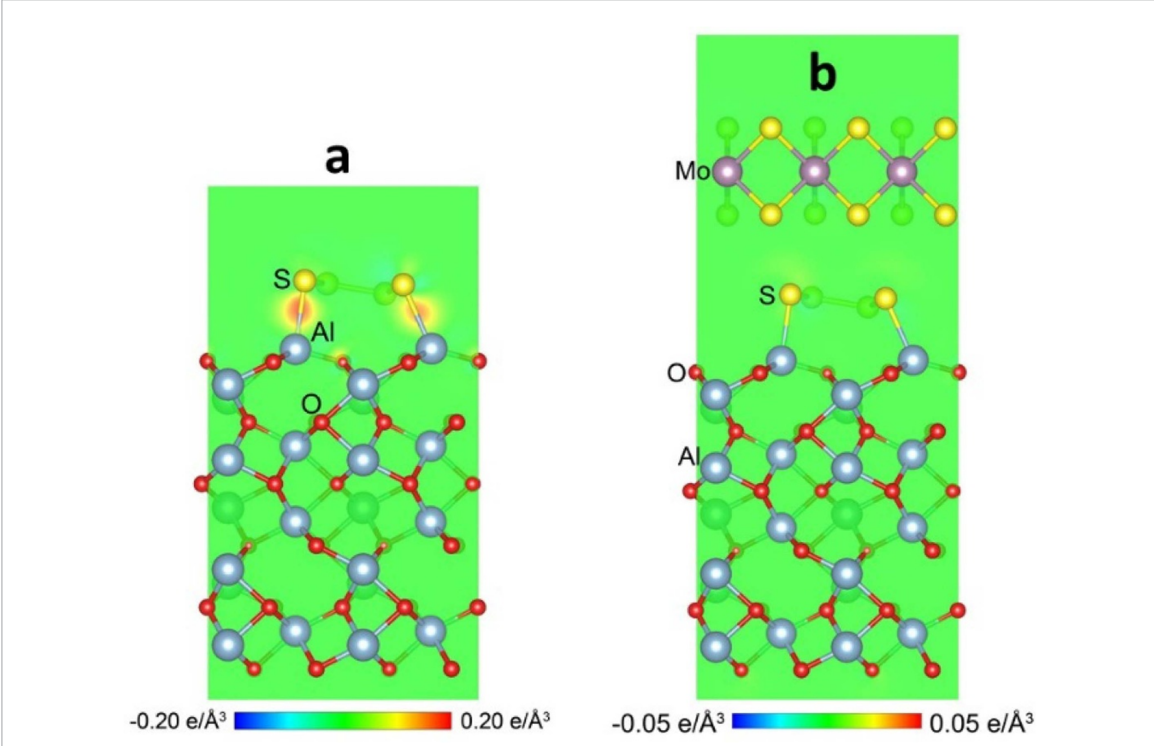

Figure 6. Charge transfer distribution slicing through (a) the plane of S passivation layer and sapphire with a scale bar from −0.20 to +0.20 e Å^{-3} and (b) the plane of MoS_2 and S passivation layer. Note the scale bar range is weaker from −0.05 to +0.05 e Å^{-3}. The solid balls are atoms in this sliced plane and the greenish balls are atoms behind the sliced plane. A positive value means gaining electrons and a negative value means losing electrons.

From RHEED, AFM, TEM, and DFT analyses we suggest that the ~3 Å serves as a van der Waals gap from the bottom S layer in ML MoS_2 to an S passivation layer. The spacing from passivation layer to sapphire is ~2 Å. A relaxed 2D van der Waals layer will grow hetero-epitaxially on a weakly interacting substrate, that is the passivated sapphire surface. We have calculated the adsorption energy of S atom at the sapphire termination as well as the interfacial interaction energy between the MoS_2 and S passivated

sapphire. The DFT result shows the charge transfer distribution at the interface between S passivation layer and Al surface as well as between MoS_2 and the S passivation layer. It is seen that the interaction between MoS_2 and the S passivation layer is very weak and is of van der Waals type. The passivation of the sapphire surface by an S layer is energetically feasible and will promote the growth of the a relaxed MoS_2 layer. During the MOCVD growth of MoS_2 ML, hydrogen sulfide (H_2S) and molybdenum hexacarbonyl ($Mo(CO)_6$) were used. The residue S could remain on the sapphire surface and facilitates the growth of MoS_2 ML. Literatures show that the van der Waals epitaxial growth of 2D layered $MoSe_2$ or $NbSe_2$ on lattice mismatched GaAs(111) 3D substrate can start with the lattice constant of $MoSe_2$ or $NbSe_2$ from the first layer of growth if the GaAs surface is passivated with S [48]. Ueno *et al* also demonstrated GaSe can be grown heteroepitaxially on an Se terminated GaAs(111) substrate by selenium vapor in the growth chamber of GaSe [49]. As stated before, Lin *et al* has shown that van der Waals WSe_2 layer can be grown on Se passivated sapphire [16]. We believe this S passivation also occurs on sapphire surface and promotes the van der Waals epitaxy of the ML MoS_2.

3. Conclusion

The 3D reciprocal space mapping using ARHEED has provided rich structural information about ML TMDCs on sapphire substrates. First, we measured the in-plane lattice constant of ML TMDCs and its epitaxial relationship with sapphire: $\{11\bar{2}0\}_{MoS2}//\{11\bar{2}0\}_{Sapphire}$. Second, from RHEED and STEM we suggest the existence of an S passivation layer at the MoS_2–sapphire interface. The spacing between TMDC bottom S layer and S passivation layer is measured to be ~3 Å and further verified with AFM height profile measurements and DFT calculations. Third, from the detailed analysis of 3D reciprocal space map, we identified that the major contribution to the broadening/splitting from azimuthal scan of diffraction spots in the RHEED patterns from ML MoS_2 to be the angular dispersion of orientation domains caused by the meandering of steps in the sapphire substrate. To sum up, we demonstrated that ARHEED is a sensitive tool to probe the structure of ML TMDCs, and can be used to evaluate wafer-scale perfection by analyzing the 3D reciprocal space map.

4. Methods

4.1. MoS_2 and WS_2 growth on c-sapphire by MOCVD

ML MoS_2 and ML WS_2 were deposited on epi-ready 2 inch *c*-sapphire substrates by MOCVD. Uniform ML deposition was achieved in a cold wall horizontal reactor equipped with wafer rotation [50]. The sapphire substrate was heated on an inductively heated graphite susceptor. $Mo(CO)_6$, tungsten hexacarbonyl ($W(CO)_6$) and H_2S were used for the growth. $Mo(CO)_6$ and $W(CO)_6$ were maintained in a stainless steel bubbler at 10 °C and 950 Torr and 760 Torr, respectively to achieve the required vapor pressure. H_2 carrier gas (10 sccm) was used to deliver 3.6×10^{-2} sccm of $Mo(CO)_6$ and 6.4×10^{-6} sccm of $W(CO)_6$ into the reaction chamber. H_2S (400 sccm) was used for the process. MoS_2 deposition was carried out at 1000 °C and 50 Torr in H_2 ambient. The substrate was first heated to 1000 °C in H_2 and maintained for 10 min before introducing the precursors for 18 min to achieve ML growth. WS_2 deposition was carried out by a modified three-step process to achieve ML growth with minimal bilayer in 12 min [11]. The reactor was then cooled down in H_2S to 300 °C to inhibit decomposition of the MoS_2 and WS_2 films. At 150 °C the system was pumped down and purged with N_2 to remove any toxic gases before unloading the wafer.

4.2. Characterizations

In order to measure the thickness and morphology of ML MoS_2 and WS_2, AFM (Bruker) was used in the peak force mode. The peak force used was 1.2 nN. To obtain the morphology of the films, 5 ×5 μm regions were scanned. Each ML sample was further examined by scanning electron microscopy (SEM), Raman spectroscopy, XPS, and PL. The Raman and PL spectra are consistent with that of ML TMDC reported in the literature. The in-plane relationship between ML MoS_2 and sapphire was verified using GIXRD [36]. RHEED was carried out in the high vacuum chamber (pressure ~10^{-8} Torr). The incident energy and glancing incident angle of electron beam used were 20 keV and ~1°, respectively. The 3D reciprocal space map was constructed from azimuthal RHEED [20]. The cross-section TEM samples were prepared using an FIB technique in FEI SEM Helios Nanolab 660. The HRTEM imaging condition for the cross section of MoS_2/sapphire interfaces was tuned to a negative Cs to provide white atom contrast at a slight over focus. Aberration-corrected STEM imaging and electron dispersive spectroscopy (EDS) (using a SuperX EDS detector) were performed by FEI Titan G2 60-300 microscope, operating at 80 kV with a double spherical aberration correction, offering a sub-angstrom imaging resolution. A HAADF detector was used for the ADF-STEM imaging with a collection angle of 51–300 mrad, a beam current of 45 pA, and a beam convergence angle of 30 mrad (C2 aperture of 70 μm) for STEM image acquisition. XPS spectra were collected using a Physical Electronics Versa Probe II instrument equipped with a monochromatic Al kα x-ray source (Energy hν = 1486.7 eV) and a concentric hemispherical

analyzer. The angle of emission (angle between incident x-ray beam and electron analyzer) was 45°. Measurements of photoelectrons were made at a takeoff angle of 45° with respect to the sample surface plane.

4.3. High-angle annular dark-field-STEM simulations

Atomic-resolution HAADF-STEM image simulations were conducted by using the QSTEM package [51]. We built the lattice model based on the atomic structure given by DFT shown in figure 5(e). We have applied the same parameters as used in the actual experimental conditions, namely: a collection angle of 51–300 mrad, a beam current of 45 pA, and a beam convergence angle of 30 mrad (C2 aperture of 70 μm).

4.4. DFT calculations

The DFT calculations were carried out with the Vienna *ab initio* Simulation Package [52]. The core electrons were described by the projector-augmented-wave method [53] and the electron exchange and correlation were modeled within the generalized gradient approximation using the Perdew–Burke–Ernzerhof form [54]. The non-local optB86b-vdW exchange-correlation functional was used to describe the dispersion interaction (vdW forces) [55, 56]. The plane wave basis kinetic energy cut off was set to 400 eV. For the construction of a supercell, the experimental and GSAM simulated results were used as references. Specifically, the alignment of TMDC and *c*-sapphire was set as parallel epitaxy ($\phi_R = 0°$). The lateral size of the supercell was set as three unit lengths of TMDC coupled with two unit lengths of *c*-sapphire. The vertical size of the supercell was set as an ML TMDC (e.g. S–Mo–S) and a unit cell size of S passivated sapphire with a vacuum gap larger than 10 Å.

We have calculated the adsorption energy of S atom at the sapphire termination as well as the interfacial interaction energy between the MoS_2 and S passivated sapphire. The S adsorption energy E_{ad} was calculated using the equation, $E_{ad} = (E_{S\text{-sapphire}} - E_{sapphire} - E_S)/N$, where, $E_{S\text{-sapphire}}$ is the energy (−770.53 eV) of sapphire with an S passivation layer, $E_{sapphire}$ is the energy (−755.33 eV) of sapphire, E_S is the energy (−13.16 eV) of S passivation layer, and $N = 4$ is the number of S atoms in the S passivation layer. The quite negative value of S atom adsorption energy (−0.51 eV) from the above equation indicates that the S passivation layer formed at the sapphire termination is energetically feasible. The strong adsorption of S passivation layer could also be confirmed by the intensive charge transfer between the S passivation layer and sapphire as shown in positive value of bright red and orange cloud in figure 6(a). This indicates the S atoms form strong bonds with Al atoms when the S atoms are adsorbed on the sapphire.

We also considered the interfacial interaction energy E_{int} between the MoS_2 and S passivated sapphire according to the equation, $E_{int} = (E_{MoS_2/S-sapphire} - E_{S-sapphire} -)/A$, where, $E_{MoS_2/S-sapphire}$ is the energy (−946.98 eV) of MoS_2–sapphire with an S passivation layer at the interface, $E_{S\text{-sapphire}}$ is the energy (−770.53 eV) of sapphire with an S passivation layer, E_{MoS_2} is the energy (−175.41 eV) of MoS_2 layer, and A is the area (78.42 Å^2) of MoS_2/S-sapphire interface. The negative value of interfacial interaction energy (−13.3 meV Å^{-2}) indicates that the MoS_2 layer could be adsorbed on the S passivated sapphire with a weak interaction. This interaction could be considered as van der Waals interaction. In contrast to figure 6(a), in figure 6(b) one can hardly see any color contrast related to charge transfer between MoS_2 and S atom implying weak bonds.

Our DFT calculations suggest that the formation of S passivation layer at the MoS_2–sapphire interface is energetically feasible. The S passivation layer is easily adsorbed on sapphire due to the quite negative adsorption energy of S atom, and the interfacial interaction energy calculation also demonstrates that the MoS_2 could be adsorbed on S passivated sapphire. As a result, the MoS_2/S-sapphire interface is stable from the aspect of energy, which also supports the experimental observation.

Acknowledgments

This work is supported by the New York State's Empire State Development's Division of Science, Technology and Innovation (NYSTAR) through Focus Center Contract C150117 and the Penn State 2D Crystal Consortium—Materials Innovation Platform under National Science Foundation cooperative agreement DMR-1539916. Y Ma and L Gao are supported by National Key Research and Development Program of China (Grant No. 2017YFB0702100) and National Natural Science Foundation of China (Grant Nos. 51705017, U1706221). We thank R Xie, T Tao, and J Liu for part of data analysis and J Meese for the construction of the 3D reciprocal map of MoS_2.

ORCID iDs

Yu Xiang https://orcid.org/0000-0001-8352-056X
Xin Sun https://orcid.org/0000-0001-5633-3371
Fu Zhang https://orcid.org/0000-0003-1841-5880
Joan M Redwing https://orcid.org/0000-0002-7906-452X
Mauricio Terrones https://orcid.org/0000-0003-0010-2851
Yuan Ma https://orcid.org/0000-0002-5982-8860
Lei Gao https://orcid.org/0000-0001-8555-5168
Gwo-Ching Wang https://orcid.org/0000-0003-1875-3345

References

[1] Splendiani A, Sun L, Zhang Y, Li T, Kim J, Chim C-Y, Galli G and Wang F 2010 Emerging photoluminescence in monolayer MoS_2 *Nano Lett.* **10** 1271–5

[2] Lee C, Yan H, Brus L E, Heinz T F, Hone J and Ryu S 2010 Anomalous lattice vibrations of single- and few-layer MoS_2 *ACS Nano* **4** 2695–700

[3] Radisavljevic B, Radenovic A, Brivio J, Giacometti V and Kis A 2011 Single-layer MoS_2 transistors *Nat. Nanotechnol.* **6** 147–50

[4] Lee Y-H *et al* 2012 Synthesis of large-area MoS_2 atomic layers with chemical vapor deposition *Adv. Mater.* **24** 2320–5

[5] Shi Y *et al* 2012 Van der Waals epitaxy of MoS_2 layers using graphene as growth templates *Nano Lett.* **12** 2784–91

[6] Wu S, Huang C, Aivazian G, Ross J S, Cobden D H and Xu X 2013 Vapor–solid growth of high optical quality MoS_2 monolayers with near-unity valley polarization *ACS Nano* **7** 2768–72

[7] Dumcenco D *et al* 2015 Large-area epitaxial monolayer MoS_2 *ACS Nano* **9** 4611–20

[8] Li H, Zhang Q, Yap C C R, Tay B K, Edwin T H T, Olivier A and Baillargeat D 2012 From bulk to monolayer MoS_2: evolution of Raman scattering *Adv. Funct. Mater.* **22** 1385–90

[9] Desai S B *et al* 2016 Gold-mediated exfoliation of ultralarge optoelectronically-perfect monolayers *Adv. Mater.* **28** 4053–8

[10] Yu H *et al* 2017 Wafer-Scale growth and transfer of highly-oriented monolayer MoS_2 continuous films *ACS Nano* **11** 12001–7

[11] Choudhury T H, Zhang X, Balushi Z Y A, Chubarov M and Redwing J M 2020 Epitaxial growth of two-dimensional layered transition metal dichalcogenides *Annu. Rev. Mater. Res.* **50** 155–77

[12] Kong D, Wang H, Cha J J, Pasta M, Koski K J, Yao J and Cui Y 2013 Synthesis of MoS_2 and $MoSe_2$ films with vertically aligned layers *Nano Lett.* **13** 1341–7

[13] Chamlagain B and Khondaker S I 2020 Electrical properties tunability of large area MoS_2 thin films by oxygen plasma treatment *Appl. Phys. Lett.* **116** 223102

[14] Ghosh S, Withanage S S, Chamlagain B, Khondaker S I, Harish S and Saha B B 2020 Low pressure sulfurization and characterization of multilayer MoS_2 for potential applications in supercapacitors *Energy* **203** 117918

[15] Rosenberger M R, Chuang H-J, McCreary K M, Li C H and Jonker B T 2018 Electrical characterization of discrete defects and impact of defect density on photoluminescence in monolayer WS_2 *ACS Nano* **12** 1793–800

[16] Lin Y-C *et al* 2018 Realizing large-scale, electronic-grade two-dimensional semiconductors *ACS Nano* **12** 965–75

[17] Wang S, Lee G-D, Lee S, Yoon E and Warner J H 2016 Detailed atomic reconstruction of extended line defects in monolayer MoS_2 *ACS Nano* **10** 5419–30

[18] Edelberg D *et al* 2019 Approaching the intrinsic limit in transition metal diselenides via point defect control *Nano Lett.* **19** 4371–9

[19] Briggs N *et al* 2019 A roadmap for electronic grade 2D materials *2D Mater.* **6** 022001

[20] Xiang Y, Guo F W, Lu T-M and Wang G-C 2016 Reflection high-energy electron diffraction measurements of reciprocal space structure of 2D materials *Nanotechnology* **27** 485703–8

[21] Lu Z H, Sun X, Xiang Y, Washington M A, Wang G-C and Lu T-M 2017 Revealing the crystalline integrity of wafer-scale graphene on SiO_2/Si: an azimuthal RHEED approach *ACS Appl. Mater. Interfaces* **9** 23081–91

[22] Zhang X, Choudhury T H, Chubarov M, Xiang Y, Jariwala B, Zhang F, Alem N, Wang G-C, Robinson J A and Redwing J M 2018 Diffusion-controlled epitaxy of large area coalesced WSe_2 monolayers on sapphire *Nano Lett.* **18** 1049–56

[23] Satapathy D K, Jenichen B, Ploog K H and Braun W 2011 Azimuthal reflection high-energy electron diffraction study of MnAs growth on GaAs(001) by molecular beam epitaxy *J. Appl. Phys.* **110** 023505

[24] Henzler M 1982 LEED studies of surface imperfections *Appl. Surf. Sci.* **11-12** 450–69

[25] Meyer G, Wollschlager J and Henzler M 1990 Epitaxial growth of thin copper layers on Cu(111) studied by high-resolution low-energy-electron diffraction *Surf. Sci.* **231** 64–75

[26] Henzler M 1984 Measurement of surface defects by low-energy electron diffraction *App. Phys.* A **34** 205–14

[27] Chen L, Dash J, Su P, Lin C F, Bhat I, Lu T-M and Wang G-C 2014 Instrument response of reflection high energy electron diffraction pole figure *Appl. Surf. Sci.* **288** 458–65

[28] Drotar J T, Lu T-M and Wang G-C 2004 Real-time observation of initial stages of copper film growth on silicon oxide using reflection high-energy electron diffraction *J. Appl. Phys.* **96** 7071–9

[29] Sung S H, Schnitzer N, Brown L, Park J and Hovden R 2019 Stacking, strain, and twist in 2D materials quantified by 3D electron diffraction *Phys. Rev. Mater.* **3** 064003

[30] Cuccureddu F, Murphy S, Shvets I V, Porcu M, Zandbergen H W, Sidorov N S and Bozhko S I 2010 Surface morphology of c-plane sapphire (α-alumina) produced by high temperature anneal *Surf. Sci.* **604** 1294–9

[31] Kurnosikov O, Van L and Cousty J 2000 High-temperature transformation of vicinal (0001) Al_2O_3-α surfaces: an AFM study *Surf. Interface Anal.* **29** 608–13

[32] Heffelfinger J R, Bench M W and Carter C B 1997 Steps and the structure of the (0001) α-alumina surface *Surf. Sci.* **370** L168–72

[33] Wang R, Guo D, Xie G and Pan G 2016 Atomic step formation on sapphire surface in ultra-precision manufacturing *Sci. Rep.* **6** 29964

[34] Chen L, Liu B, Ge M, Ma Y, Abbas A N and Zhou C 2015 Step-edge-guided nucleation and growth of aligned WSe_2 on sapphire via a layer-over-layer growth mode *ACS Nano* **9** 8368–75

[35] Zhao Y-P, Wang G-C and Lu T-M 2001 Characterization of amorphous and crystalline rough surface: principles and applications *Experimental Methods in the Physical Science* (New York: Academic) vol 37 pp 8

[36] Chubarov M, Choudhury T H, Zhang X and Redwing J M 2018 In-plane x-ray diffraction for characterization of monolayer and few-layer transition metal dichalcogenide films *Nanotechnology* **29** 055706

[37] Yang H N, Fang K, Wang G C and Lu T M 1991 Vacancy-induced disordering in the Pb(100) surface *Phys. Rev.* B **44** 1306–10

[38] Mignuzzi S, Pollard A J, Bonini N, Brennan B, Gilmore I S, Pimenta M A, Richards D and Roy D 2015 Effect of disorder on Raman scattering of single-layer MoS_2 *Phys. Rev.* B **91** 195411

[39] Spadacini R and Tommei G E 1983 A Markovian approach to atomic scattering from rough surfaces *Surf. Sci.* **133** 216–32

[40] 2DCC 2020 MoS_2 on c-sapphire(0001) (available at: www.mri.psu.edu/sites/default/files/2dcc/List%20of%20Thin%20Film%20Samples%20Available%20Certification%20MoS2_modified.pdf)

[41] Meyer J C, Geim A K, Katsnelson M I, Novoselov K S, Booth T J and Roth S 2007 The structure of suspended graphene sheets *Nature* **446** 60–63

[42] Lu T-M, Wang G-C and Lagally M G 1981 Quantitative island size determination in the chemisorbed layer W(110)p(2x1)-O II. Theoretical models *Surf. Sci.* **108** 494–518

[43] Wang G-C and Lu T-M 2019 Strain measurement of ultrathin epitaxial films using electron diffraction techniques *J. Appl. Phys.* **125** 082401

[44] Mo J, El Kazzi S, Mortelmans W, Mehta A N, Sergeant S, Smets Q, Asselberghs I and Huyghebaert C 2020 Importance of the substrate's surface evolution during the MOVPE growth of 2D-transition metal dichalcogenides *Nanotechnology* **31** 125604

[45] Aljarb A, Cao Z, Tang H-L, Huang J-K, Li M, Hu W, Cavallo L and Li L-J 2017 Substrate lattice-guided seed formation controls the orientation of 2D transition-metal dichalcogenides *ACS Nano* **11** 9215–22

[46] Soares E A, Van Hove M A, Walters C F and McCarty K F 2002 Structure of the α-Al_2O_3(0001) surface from low-energy electron diffraction: al termination and evidence for anomalously large thermal vibrations *Phy. Rev.* B **65** 195405

[47] Guenard P, Renaud G, Barbier A and Gautier-Soyer M 2011 Determination of the α-Al_2O_3(0001) surface relaxation and termination by measurements of crystal truncation rods *MRS Proc.* **437** 15

[48] Ueno K, Shimada T, Saiki K and Koma A 1990 Heteroepitaxial growth of layered transition metal dichalcogenides on sulfur-terminated GaAs111 surfaces *Appl. Phys. Lett.* **56** 327–9

[49] Ueno K, Abe H, Saiki K and Koma A 1991 Heteroepitaxy of layered semiconductor GaSe on a GaAs(111)B Surface *Japan. J. Appl. Phys.* **30** L1352–4

[50] Xuan Y *et al* 2019 Multi-scale modeling of gas-phase reactions in metal-organic chemical vapor deposition growth of WSe_2 *J. Cryst. Growth* **527** 125247

[51] Koch C T 2002 Determination of core structure periodicity and point defect density along dislocations *PhD Thesis*, Arizona State University

[52] Kresse G and Furthmüller J 1996 Efficiency of *ab-initio* total energy calculations for metals and semiconductors using a plane-wave basis set *Comput. Mater. Sci.* **6** 15–50

[53] Blöchl P E 1994 Projector augmented-wave method *Phys. Rev.* B **50** 17953

[54] Perdew J P, Burke K and Ernzerhof M 1996 Generalized gradient approximation made simple *Phys. Rev. Lett.* **77** 3865

[55] Klimeš J, Bowler D R and Michaelides A 2009 Chemical accuracy for the van der Waals density functional *J. Phys.: Condens. Matter.* **22** 022201

[56] Klimeš J, Bowler D R and Michaelides A 2011 Van der Waals density functionals applied to solids *Phys. Rev.* B **83** 195131